Target Refocusing via Attention Redistribution for Open-Vocabulary Semantic Segmentation: An Explainability Perspective

Jiahao Li¹, Yang Lu¹, Yachao Zhang¹, Yong Xie^{3*}, Fangyong Wang⁴, Yuan Xie², Yanyun Qu^{1*}

¹Key Laboratory of Multimedia Trusted Perception and Eficient Computing. Ministry of Education of China, School of Informatics, Xiamen University

²School of Computer Science and Technology, East China Normal University
 ³Department of Computer, Nanjing University of Posts and Telecommunications
 ⁴Hanjiang National Laboratory

Abstract

Open-vocabulary semantic segmentation (OVSS) employs pixel-level vision-language alignment to associate categoryrelated prompts with corresponding pixels. A key challenge is enhancing the multimodal dense prediction capability, specifically this pixel-level multimodal alignment. Although existing methods achieve promising results by leveraging CLIP's vision-language alignment, they rarely investigate the performance boundaries of CLIP for dense prediction from an interpretability mechanisms perspective. In this work, we systematically investigate CLIP's internal mechanisms and identify a critical phenomenon: analogous to human distraction, CLIP diverts significant attention resources from target regions to irrelevant tokens. Our analysis reveals that these tokens arise from dimension-specific over-activation; filtering them enhances CLIP's dense prediction performance. Consequently, we propose ReFocusing CLIP (RF-CLIP), a training-free approach that emulates human distraction-refocusing behavior to redirect attention from distraction tokens back to target regions, thereby refining CLIP's multimodal alignment granularity. Our method achieves SOTA performance on eight benchmarks while maintaining high inference efficiency.

Introduction

Open-vocabulary semantic segmentation assigns categorical labels from an unrestricted vocabulary to each image pixel via prompt-guided multimodal semantic alignment. The core challenge lies in achieving pixel-level dense prediction, where fine-grained multimodal alignment constitutes a critical bottleneck. Existing approaches predominantly leverage CLIP's (Radford et al. 2021) vision-language alignment capability to address this challenge, falling into three paradigms: 1) **Joint Fine-tuning** (Cho et al. 2024; Jiao et al. 2023; Li et al. 2024): simultaneously fine-tuning CLIP alongside segmentation-specific components to enhance dense prediction capabilities; 2) **Pre Fine-tuning** (Wu et al. 2023a, 2024a; Xu et al. 2022a): refining CLIP's alignment granularity through fine-grained vision-language contrastive

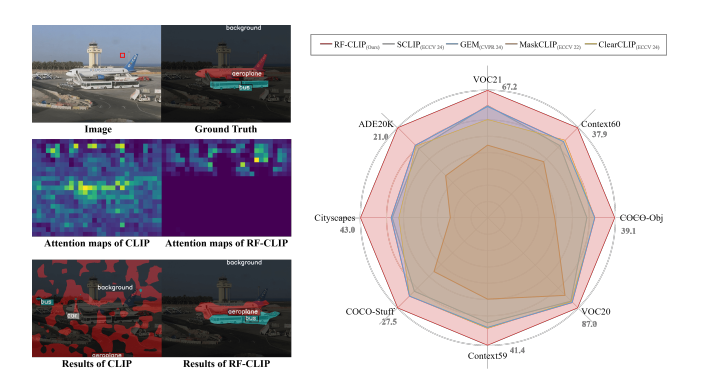


Figure 1: RF-CLIP achieves precise attention focus, which facilitates accurate segmentation of target regions. Compared to state-of-the-art methods, RF-CLIP demonstrates superior performance, achieving the highest accuracy.

learning; 3) **Training-Free Adaptation**(Lan et al. 2024a; Wang, Mei, and Yuille 2024; Lan et al. 2024b): modulating CLIP's final residual attention layer or integrating vision foundation models (VFMs)(Zhang et al. 2022; Oquab et al. 2023) to boost alignment granularity. Collectively, these paradigms deploy complementary strategies—augmenting CLIP with task-specific modules, re-pretraining weights, or adapting final layers while aggregating VFMs—all targeting enhanced multimodal alignment granularity. Despite promising results, existing methods rarely investigate the performance boundaries of CLIP for dense prediction from an interpretability perspective or explore the origins of its inherent inter-layer spatial misalignment, thereby limiting further improvements in OVSS performance.

In this work, we focus on the training-free paradigm, exclusively modulating CLIP to enhance pixel-level dense prediction. We first systematically investigate CLIP's internal mechanisms and uncover a key phenomenon: during visual encoding, CLIP produces certain tokens irrelevant to the input query that consume substantial attention resources, causing distraction from originally focused target regions (termed the "distraction" phenomenon causing layer-wise spatial misalignment). Further analysis reveals

^{*}Corresponding author.
Code: https://github.com/liblacklucy/RF-CLIP
Copyright © 2026, Association for the Advancement of Artificial
Intelligence (www.aaai.org). All rights reserved.

these tokens stem from over-activation in specific dimensions; filtering them significantly improves CLIP's OVSS performance. Their presence seems to indicate that CLIP struggles to focus on the current visual targets, impairing its dense prediction ability. This insight motivates us to explore whether mimicking the human distraction-refocusing behavior — by reallocating attention resources from distraction tokens to defocused target regions - can enhance CLIP's multimodal alignment granularity.

To this end, we propose ReFocusing CLIP (RF-CLIP), a straightforward training-free modulation method that operates directly on CLIP's inter-layer attention mechanisms. The core idea lies in: 1) identifying query-irrelevant tokens consuming substantial attention resources and locating defocused target regions within CLIP's intermediate visual embeddings; 2) reallocating attention resources from distraction tokens to these defocused target regions. By exclusively modulating CLIP's attention mechanism, RF-CLIP significantly enhances OVSS performance while preserving inference efficiency (Figure 1). Our principal contributions are:

- We identify the "distraction" phenomenon and attribute it to dimension-specific over-activation inherent in CLIP, which undermines the multimodal alignment granularity.
- We propose RF-CLIP, a training-free attention modulator that enhances alignment granularity by reallocating misallocated attention resources to defocused target regions.
- Our method achieves SOTA performance on eight OVSS benchmark datasets while simultaneously preserving superior computational efficiency during inference.

Preliminaries

Problem definition. Given an image I and a set of classspecific textual descriptions $\{T_i\}_{i=1}^{N_c}$, where T_i denotes the textual description of the i-th class and N_c represents the total number of classes, CLIP aligns each pixel in I with the most semantically relevant T_i , thereby assigning the corresponding class label i to the pixel. Note that the total number of classes N_c is dynamic during inference.

Dense inference for training-free OVSS. The ViT-based CLIP model primarily comprises multiple stacked residual attention layers. Each residual layer contains a self-attention module $S(\cdot)$ and a feedforward module $F(\cdot)$. Given an image I, a visual residual layer processes it to extract visual embeddings $f \in \mathbb{R}^{N \times d}$, where N represents the number of patches and d is the latent space dimension. (In actual, fcomprises a global visual embeddings $f' \in \mathbb{R}^{1 \times d}$ and a local dense embeddings $f'' \in \mathbb{R}^{N \times d}$; for simplicity, we refer to f as the local dense embeddings f'' and ignore the global visual embeddings). The computation process within a visual residual layer is defined as (normalization operations omitted for simplicity):

$$\mathbf{f}^{l} \leftarrow \mathbf{f}^{l} + \mathcal{S}(\mathbf{f}^{l}), \tag{1}$$
$$\mathbf{f}^{l+1} \leftarrow \mathbf{f}^{l} + \mathcal{F}(\mathbf{f}^{l}), \tag{2}$$

$$\mathbf{f}^{l+1} \leftarrow \mathbf{f}^l + \mathcal{F}(\mathbf{f}^l),$$
 (2)

where $l \in [1, L]$ denote the current layer index. The computation process of self-attention module $S(\cdot)$ is defined as:

$$S(\mathbf{f}^l) = \operatorname{Attn}_{qk}^l \cdot \mathbf{V}^l, \operatorname{Attn}_{qk}^l = \operatorname{softmax}(\frac{\mathbf{Q}^l \mathbf{K}^{l^\top}}{\sqrt{d}}), \quad (3)$$

$$Q^l = f^l W_q^l, \quad K^l = f^l W_k^l, \quad V^l = f^l W_v^l,$$
 (4)

where W_q, W_k, W_v are linear projection matrices, and Attn_{qk} are self-attention maps. Similarly, given a set of textual descriptions $\{T_i\}_{i=1}^{N_c}$, CLIP textual encoder extracts its textual embeddings $f_t \in \mathbb{R}^{N_c \times d}$. Thus, the final open-vocabulary semantic segmentation map $M \in \mathbb{R}^{H \times W}$ (or $\in \mathbb{R}^{N \times 1}$ if flattened) is:

$$M = \operatorname*{arg\,max}_{N_c} \cos{(\boldsymbol{f}^L, \boldsymbol{f}_t)}. \tag{5}$$

In addition, due to the residual connection (including the feedforward module) in the final residual layer often producing "noisy" segmentation maps (Lan et al. 2024a), the output of its self-attention module is typically used as the final output visual embeddings f^L . The computation within the last visual residual layer is: $f^L \leftarrow \mathcal{S}(f^{L-1})$.

Training-free adaptation for OVSS. Omission of the residual connection in the final layer and reliance solely on $S(\cdot)$ markedly enhance the perceptual granularity of visual embeddings. Consequently, existing research focuses on refining $\mathcal{S}(\cdot)$ to achieve finer-grained spatial alignment. These methods primarily aim to optimize the final self-attention matrices $\operatorname{Attn}_{q,k}^L \in \mathbb{R}^{N \times N}$ for more precise modeling of local spatial relationships among image patches. They fall into two main categories:

- VFM-proxy. These methods leverage the dense representation capabilities of powerful visual foundation models to enhance CLIP. ProxyCLIP (Lan et al. 2024b) utilizes DINO (Zhang et al. 2022)'s visual representations to compute self-similarity, replacing CLIP's original selfattention matrices. CASS (Kim et al. 2025) employs spectral graph distillation to integrate DINO's dense visual features, thereby strengthening CLIP's contextual coherence.
- Self-proxy. They construct novel self-attention matrices from their own embeddings, replacing the original $\operatorname{Attn}_{q,k}^L$. For instance, SCLIP (Wang, Mei, and Yuille 2024) utilizes the summation of $\operatorname{Attn}_{qq}^L$ and $\operatorname{Attn}_{kk}^L$ as the final self-attention matrix. ClearCLIP (Lan et al. 2024a) and NACLIP (Hajimiri, Ayed, and Dolz 2025) respectively substitute $\operatorname{Attn}_{qk}^L$ with $\operatorname{Attn}_{qq}^L$ and $\operatorname{Attn}_{kk}^L$. Later we refer to Attn_{kk} -proxy CLIP as CLIP with $\operatorname{Attn}_{kk}^L$ replacing $Attn_{ak}^L$.

Despite the impressive achievements of the aforementioned paradigms, they exhibit a fundamental limitation: these approaches exclusively modulate the final residual attention layer (to prevent model collapse), while ignoring patch-level spatial misalignments within intermediate residual layers. This oversight causes accumulated error propagation across the network. This raises a critical question: Could direct correction of spatial misalignments in intermediate residual layers enhance CLIP's dense prediction performance? To this

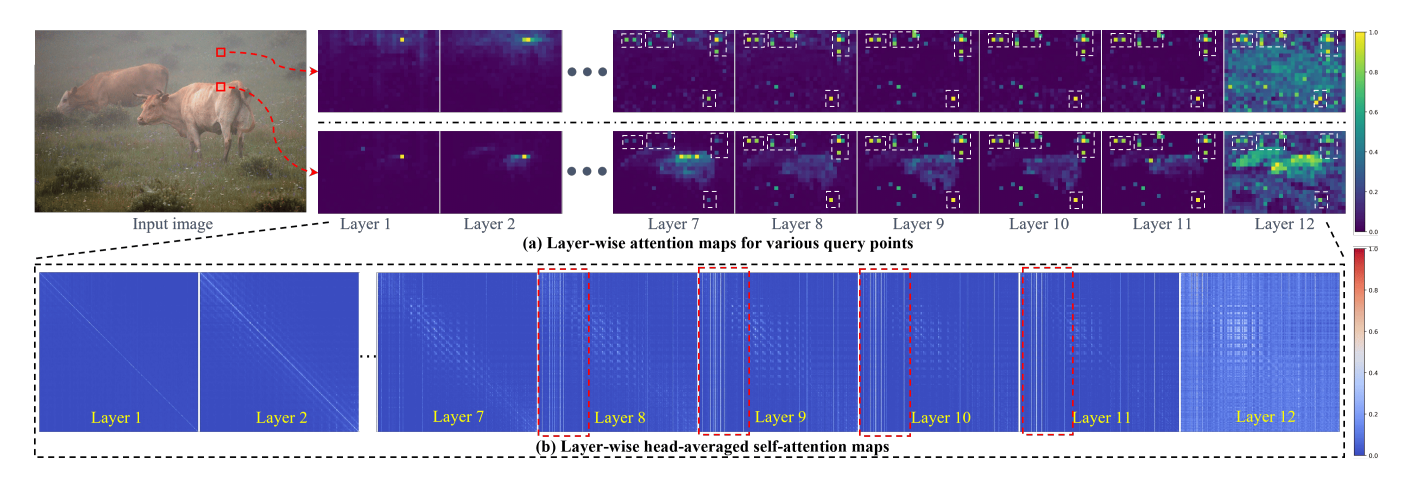


Figure 2: Illustration of "distraction" phenomenon. (a) Layer-wise attention maps for two query locations reveal query-to-tokens relevance across the entire image. (b) Layer-wise head-averaged self-attention maps characterize token-to-token relationships. Red solid boxes denote query points; white dashed boxes indicate distraction tokens; and red dashed boxes represent attention weights of distraction tokens.

end, in the next section, we systematically analyze the selfattention matrices layer-wise to probe CLIP's underlying mechanisms from an interpretability perspective.

"Distraction" phenomenon

In this section, we first delineate the "distraction" phenomenon, which reveals pronounced spatial misalignment artifacts within CLIP. Furthermore, our empirical analysis establishes that this phenomenon originates from excessive activation in specific dimensions. Building on this analysis, we precisely identify distraction tokens. Finally, we systematically evaluate diverse suppression strategies on these distraction tokens, thereby inspiring our proposed method.

Key observations. Figure 2 presents layer-wise attention maps $\operatorname{Attn}_{qk}^{l}[i]$ capturing token relevance to diverse query points i, alongside head-averaged self-attention maps revealing token-to-token relationships. Attention maps visualization (Figure 2 (a)) demonstrates that shallow layers (1-2) predominantly attend to query-relevant tokens. In contrast, deeper layers (7-12) exhibit numerous high-attention tokens unrelated to target queries (demarcated by white dashed boxes) - a phenomenon we term "distraction," with these tokens designated as distraction tokens \mathcal{T}_{dis} . The emergence of distraction tokens progressively diminishes saliency around query-related regions, defocusing originally concentrated target areas. Crucially, these distraction tokens consistently occupy identical spatial positions across two varying query points, perhaps suggesting their universal correlations with all queries points. Self-attention maps visualization (Figure 2 (b)) corroborate this behavior: distraction tokens manifest distinct vertical stripes (within red dashed boxes) due to uniformly high attention values between all tokens and them, i.e., their attention weights $\sum_{i} \operatorname{Attn}_{qk}^{l}[j,i]_{,i \in \mathcal{T}_{dis}}$ are large, reflecting the sum of the relevance of them to all tokens. Therefore, these tokens fundamentally induce spatial misalignment, propagating errors through residual layers,

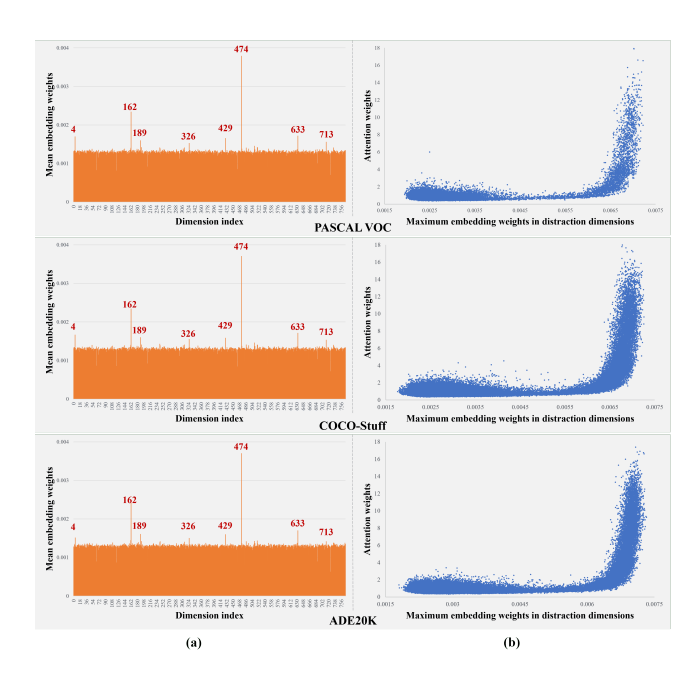
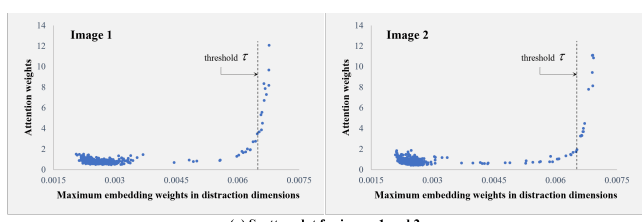


Figure 3: Weights analysis. (a) Histogram of per-dimension mean embedding weights averaged across the entire dataset. (b) Scatter plot of tokens' attention weights versus their maximum embedding weights in distraction dimensions.

and ultimately constraining CLIP's dense prediction ability.

How do distraction tokens surface? Given distraction tokens' persistent high correlation with all tokens, we hypothesize they exhibit massive embedding weights. We compute visual dense embeddings averaged across residual layers as: $\bar{f} = \frac{1}{L} \sum_{l=1}^{L} (\frac{f^l}{\sum_{j=1}^{d} f^l[:,j]}) \in \mathbb{R}^{N \times d}$, where L denotes total layers. The embedding weights of i-th token in j-th dimension can be defined as $\bar{f}[i,j]$, representing its weights distri-



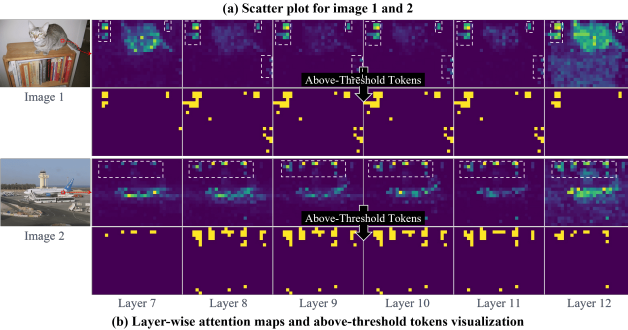


Figure 4: Distraction tokens identification. (a) Scatter plot of attention weights versus maximum embedding weights in \mathcal{D}_{dis} . (b) Layer-wise attention maps and above-threshold tokens visualizations.

bution across diverse dimensions. Figure 3 (a) displays the mean embedding weights averaged across the entire dataset, reflecting the weights distribution of the entire dataset in CLIP's high-dimensional space. We find that three largescale OVSS benchmark datasets exhibit consistent weights distribution, with several peaks at identical dimensions (e.g., 4, 162, 474, etc., denoted red), which we designate as distraction dimensions \mathcal{D}_{dis} . This indicates CLIP intrinsically generates massive embedding weights in \mathcal{D}_{dis} — an inherent property independent of dataset specifics. Figure 3 (b) validates our hypothesis, plotting for each token i: Attention weights $(\sum_{i} Attn[j, i]^{1})$ and Maximum embedding weights ϕ_i in \mathcal{D}_{dis} ($\dot{\phi}_i = \max_{j \in \mathcal{D}_{dis}} \bar{f}[i,j]$). We observe that tokens with massive ϕ_i consistently exhibit high attention weights, and that growth in ϕ_i causes exponential growth in attention weights. Therefore, we conclude that tokens with massive maximum embedding weights in the distraction dimensions inevitably evolve into distraction tokens under selfattention calculation mechanisms.

Where are distraction tokens? Building upon the above analysis, we define $\tau=5/d$ as the identification threshold, where token i satisfying $\phi_i>\tau$ are identified as distraction tokens. As shown in Figure 4 (a), the scatter plot maps of two images show that above-threshold tokens exhibit high attention weights. Figure 4 (b) visually confirms these tokens' spatial distribution, revealing near-perfect alignment with observed distraction patterns. Therefore, distraction token identification reduces to a simple threshold operation on maximum embedding weights within \mathcal{D}_{dis} .

Method	VOC21	COCO-Stuff	Cityscapes	ADE20k	Avg.
baseline	58.1	23.0	31.1	16.3	32.1
-∞ masking	3.5 (-54.6)	0.1 (-22.9)	2.0 (-29.1)	0.1 (-16.2)	1.4
low-pass filtering	7.9 (-50.2)	1.1 (-21.9)	6.2 (-24.9)	1.4 (-14.9)	4.2
mean filtering	59.3 (+1.2)	24.0 (+1.0)	35.4 (+4.3)	18.2 (+1.9)	34.2
median filtering	58.6 (+0.5)	23.7 (+0.7)	34.5 (+3.4)	17.6 (+1.3)	33.6

Table 1: Quantitative evaluation for four suppression strategies (unit: %). Red and green fonts denote descending and ascending values. Baseline: Attn_{kk}-proxy CLIP.

Suppression strategies on distraction tokens. To explore whether suppressing distraction tokens enhances CLIP's dense prediction capability, we establish an $Attn_{kk}$ -proxy CLIP baseline and evaluate four suppression strategies: $-\infty$ masking² - nullifying layer-wise distraction tokens embeddings, low-pass filtering - clamping these embeddings to τ , mean filtering - replacing with mean of 3×3 local neighborhoods, and median filtering - substituting with median of 3×3 neighborhoods. As shown in Table 1, both $-\infty$ masking and low-passing filtering degrade performance, whereas mean and median filtering yield measurable improvements. This indicates that distraction tokens should maintain spatial consistency with adjacent regions: Direct elimination disrupts the topological structure of CLIP's high-dimensional space, inducing model collapse. Consequently, we are motivated to investigate whether reallocating attention resources from distraction tokens to defocused target regions can enhance CLIP's dense prediction capability.

Approach

Our objective is to improve CLIP's dense prediction performance by mitigating layer-wise spatial misalignment. Building on the above analysis, we introduce $\underline{\text{ReF}}$ ocusing CLIP (RF-CLIP) – a training-free approach that simulates human distraction-refocusing behavior to redirect layer-wise scattered attention resources toward defocused target regions. As shown in Figure 5, RF-CLIP consists of three key components: (a) Distractor Localization, identifying attention-rich distraction tokens; (b) Defocus Localization, detecting attention-poor defocused tokens; (c) Weight Redistribution, refocusing distracted attention back to defocused target tokens. Below, we use the l-th residual layer as an illustrative example to elucidate these components.

Distractor localization. Given the input embedding $f_i^l \in \mathbb{R}^d$ of the *i*-th visual token, we define its maximum embedding weight in the distraction dimensions can be defined as:

$$\phi_i^l = \max_{j \in \mathcal{D}_{dis}} \frac{\boldsymbol{f}_i^l[j]}{\sum_{k=1}^d \boldsymbol{f}_i^l[k]}$$
(6)

Using the threshold $\tau=5/d$, we identify distraction tokens statisfying $\phi_i^l>\tau$.

Defocus localization. We conceptualize defocused tokens as foreground instances and formulate defocus localization

 $^{^{1}}$ Here, $\mathrm{Attn}=\frac{1}{L\cdot H}\sum_{l,h=1}^{l,h=L,H}\mathrm{Attn}_{qk}^{l,h}$ denotes self-attention matrices averaged across all L layers and H heads.

 $^{^2-\}infty$ forces softmax-attention value to zero

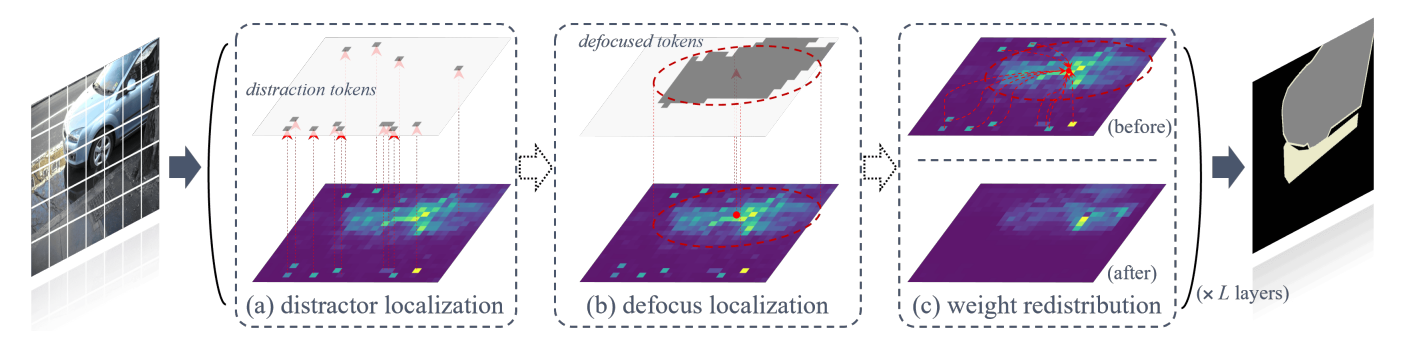


Figure 5: Overview of RF-CLIP. Our RF-CLIP directly correct layer-wise spatial misalignment in CLIP to enhance dense prediction capabilities. Each layer's correction mechanism comprises three key components: (a) distractor localization, identifying attention-rich distraction tokens irrelevant to target objects; (b) defocus localization, detecting attention-poor defocused tokens relevant to targets; (c) weight redistribution, reallocating attention resources from distraction tokens to defocused tokens.

as a bipartition graph cut problem. Adopting spectral clustering on the similarity matrix $\operatorname{Attn}_{kk}^l$, we represent each token i as a node n_i , partitioning the graph into foreground ${\cal A}$ and background ${\cal B}$ sets. This optimization problem aims to minimize the normalized cut energy:

$$\frac{\mathcal{E}(\mathcal{A},\mathcal{B})}{\mathcal{E}(\mathcal{A},\mathcal{V})} + \frac{\mathcal{E}(\mathcal{A},\mathcal{B})}{\mathcal{E}(\mathcal{B},\mathcal{V})}, \quad \mathcal{V} = \mathcal{A} \cup \mathcal{B}, \tag{7}$$

where $\mathcal{E}(\cdot,\cdot)$ denotes set similarity. Using key-key attention $\operatorname{Attn}_{kk}^l$ as token-wise similarity measure, we define $\mathcal{E}(\mathcal{A}, \mathcal{B}) = \sum_{n_i \in \mathcal{A}, n_j \in \mathcal{B}} \operatorname{Attn}_{kk}^l[i, j]$. Following Shi and Malik (2000), Equation 7 is optimized by solving:

$$\boldsymbol{y}_{1}^{l} = \underset{\boldsymbol{y}^{l^{\top}}\boldsymbol{D}\mathbf{1}=0}{\operatorname{arg\,min}} \frac{\boldsymbol{y}^{l^{\top}}(\boldsymbol{D}^{l} - \operatorname{Attn}_{kk}^{l})\boldsymbol{y}^{l}}{\boldsymbol{y}^{l^{\top}}\boldsymbol{D}^{l}\boldsymbol{y}^{l}},$$
(8)

where $\boldsymbol{y}_1^l \in \mathbb{R}^N$ denotes the Fiedler vector — the eigenvector corresponding to the second smallest eigenvalue of the generalized eigensystem $(\boldsymbol{D}^l - \operatorname{Attn}_{kk}^l) \boldsymbol{y}^l = \lambda \boldsymbol{D}^l \boldsymbol{y}^l$. Here, \boldsymbol{D} is a diagonal matrix with $\sum_j \operatorname{Attn}_{kk}^l[:,j]$ on its diagonal. Thus, defocused tokens are identified as those satisfying $y_1^l[i] > \frac{1}{N} \sum_{j=1}^N y_1^l[j]$.

Weight redistribution. We formalize weight redistribution through two complementary mechanisms: (1) attention weight redistribution across spatial locations, and (2) embedding weight redistribution across embedding dimensions. Let \mathcal{T}_{dis} and \mathcal{T}_{def} denote the sets of distraction tokens and defocused tokens, respectively. The attention redistribution process transfers attention weights from \mathcal{T}_{dis} to \mathcal{T}_{def} while preserving original contribution distribution, thereby maintaining the topological structure of layer-wise self-attention matrices and preventing model collapse. This is achieved through two sequential operations. First. attention weights for distraction tokens are scaled down, with the decrement preserved as a redistribution budget Ω :

$$\operatorname{Attn}_{qk}^{l,h}[i,j] \leftarrow (1-\beta) \cdot \operatorname{Attn}_{qk}^{l,h}[i,j], \forall j \in \mathcal{T}_{dis}, \quad (9)$$

$$\operatorname{Attn}_{qk}^{l,h}[i,j] \leftarrow (1-\beta) \cdot \operatorname{Attn}_{qk}^{l,h}[i,j], \forall j \in \mathcal{T}_{dis}, \qquad (9)$$

$$\Omega[i] = \beta \cdot \sum_{j \in \mathcal{T}_{dis}} \operatorname{Attn}_{qk}^{l,h}[i,j], \qquad (10)$$

where $\beta \in (0,1)$ is the attenuation factor. Second, the budget is distributed to defocused tokens proportional to their original attention weights:

$$\operatorname{Attn}_{qk}^{l,h}[i,j] \leftarrow \operatorname{Attn}_{qk}^{l,h}[i,j] + \Omega[i] \cdot \rho[i,j], \forall j \in \mathcal{T}_{def}, \quad (11)$$

$$\rho[i,j] = \frac{\operatorname{Attn}_{qk}^{l,h}[i,j]}{\sum_{j \in \mathcal{T}_{def}} \operatorname{Attn}_{qk}^{l,h}[i,j]},$$
(12)

where ρ represents the original contribution distribution determining each defocused token's allocation share. This process maintains column-normalization $(\sum_{j} \operatorname{Attn}_{qk}^{l,h}[i,j] =$ 1) and preserves the original attention distribution, thus effectively mitigating model collapse while enhancing focus on defocused tokens. The embedding redistribution process uses a local 3×3 neighborhood centered on each distraction tokens in \mathcal{T}_{dis} to compute averaged embedding representations. For dimension $j \in \mathcal{D}_{dis}$, the embedding weights are updated through spatial averaging:

$$\boldsymbol{f}_{i}^{l}[j] = \frac{1}{8} \cdot \sum_{\hat{i} \in \mathcal{O}_{i}} \boldsymbol{f}_{\hat{i}}^{l}[j], \forall j \in \mathcal{D}_{dis} \text{ and } i \in \mathcal{T}_{dis},$$
 (13)

where \mathcal{O}_i denote 3×3 neighboring regions centered token i. This process only adjusts the embedding in \mathcal{D}_{dis} without destroying the distribution in normal dimensions, thus effectively ensuring the integrity of the original embeddings.

Dense prediction. Given the layer-wise spatial misalignment correction, we replace $\operatorname{Attn}_{qk}^L$ with the layer-averaged attention $\overline{\operatorname{Attn}}_{kk} = \frac{1}{L} \sum_{l=1}^L \operatorname{Attn}_{kk}^l$ to produce the final visual embeddings. The segmentation map is computed as:

$$M = \underset{N_c}{\operatorname{arg\,max}} \cos(f^L, f_t), \quad f^L = \overline{\operatorname{Attn}}_{kk} \cdot V^L.$$
 (14)

Please refer to the Appendix for the pseudocode of RF-CLIP.

Experiments

Experiments settings. Following the existing trainingfree works, we conduct evaluations on eight standard benchmark datasets: VOC21 (Everingham et al. 2012), VOC20 (Everingham et al. 2012), Context60 (Mottaghi et al.

Model	Baseline	Additional VFM	VOC21	Context60	COCO-Obj	VOC20	Context59	COCO-Stuff	Cityscapes	ADE20K	Avg.
ReCo (Shin, Xie, and Albanie 2022)	CLIP ViT-B/16	MaskCLIP	25.1	19.9	15.7	57.7	22.3	14.8	21.6	11.2	23.5
LaVG (Kang and Cho 2024)	CLIP ViT-B/16	DINO	62.1	31.6	34.2	82.5	34.7	23.2	26.2	15.8	38.8
CLIP-DINOiser† (Wysoczańska et al. 2024)	CLIP ViT-B/16	DINO	62.1	32.4	34.8	80.9	35.9	24.6	31.7	20.0	40.3
FreeDa (Barsellotti et al. 2024)	CLIP ViT-B/16	DINOv2	-	-	-	85.6	43.1	27.8	36.7	22.4	-
ProxyCLIP [‡] (Lan et al. 2024b)	CLIP ViT-B/16	DINO	59.1	35.2	36.2	78.2	38.8	26.2	38.1	19.6	41.4
CASS (Kim et al. 2025)	CLIP ViT-B/16	DINO	65.8	36.7	37.8	87.8	40.2	26.7	39.4	20.4	<u>44.4</u>
CLIP (Radford et al. 2021)	CLIP ViT-B/16	X	18.6	7.8	6.5	49.1	11.2	7.2	6.7	3.2	13.8
MaskCLIP (Zhou, Loy, and Dai 2022)	CLIP ViT-B/16	X	38.3	23.6	20.6	74.9	26.4	16.4	12.6	9.8	27.9
GroupViT (Xu et al. 2022a)	CLIP ViT-B/16	X	50.4	18.7	27.5	79.7	23.4	15.3	11.1	9.2	29.4
CLIPtrase (Shao et al. 2024)	CLIP ViT-B/16	X	50.9	29.9	43.6	81.0	33.8	22.8	21.3	16.4	32.7
TCL (Cha, Mun, and Roh 2023)	CLIP ViT-B/16	X	55.0	30.4	31.6	83.2	33.9	22.4	24.0	17.1	37.2
CLIPSurgery (Li et al. 2023)	CLIP ViT-B/16	X	55.2	30.3	29.7	77.5	33.4	22.2	33.1	16.1	37.2
GEM (Bousselham et al. 2024)	CLIP ViT-B/16	X	58.7	32.0	32.9	81.7	35.6	23.9	32.6	16.9	39.3
CaR (Sun et al. 2024)	CLIP ViT-B/16	Х	48.6	13.6	15.4	73.7	18.4	-	-	5.4	-
ClearCLIP (Lan et al. 2024a)	CLIP ViT-B/16	Х	51.8	32.6	33.0	80.9	35.9	23.9	30.0	16.7	38.1
SCLIP (Wang, Mei, and Yuille 2024)	CLIP ViT-B/16	Х	59.1	30.4	30.5	80.4	34.1	22.4	32.2	16.1	38.2
NACLIP (Hajimiri, Ayed, and Dolz 2025)	CLIP ViT-B/16	Х	58.9	32.2	33.2	79.7	35.2	23.3	35.5	17.4	39.4
SC-CLIP (Bai et al. 2024)	CLIP ViT-B/16	Х	64.6	<u>36.8</u>	37.7	84.3	40.1	26.6	41.0	20.1	43.9
RF-CLIP (Ours)	CLIP ViT-B/16	Х	64.8	36.4	37.9	87.0	39.8	26.3	41.3	20.4	44.2
with PAMR			67.2	37.9	<u>39.1</u>	<u>87.0</u>	<u>41.4</u>	<u>27.5</u>	43.0	<u>21.0</u>	45.5
ProxyCLIP [‡] (Lan et al. 2024b)	CLIP ViT-L/14	DINO	58.1	34.1	37.4	82.0	37.3	25.5	38.1	21.2	41.7
CLIP (Radford et al. 2021)	CLIP ViT-L/14	X	10.3	4.5	4.4	19.9	5.7	3.2	3.2	1.9	6.6
MaskCLIP (Zhou, Loy, and Dai 2022)	CLIP ViT-L/14	Х	24.8	9.7	10.2	30.1	13.0	9.0	12.1	7.1	14.5
SCLIP (Wang, Mei, and Yuille 2024)	CLIP ViT-L/14	Х	44.4	22.3	24.9	70.6	25.2	16.5	21.3	10.9	29.5
GEM (Bousselham et al. 2024)	CLIP ViT-L/14	Х	45.2	25.5	28.3	83.7	28.1	19.2	27.1	13.2	33.8
CLIPSurgery (Li et al. 2023)	CLIP ViT-L/14	X	47.9	27.3	28.1	84.3	31.0	21.4	29.7	17.3	35.9
PnP-OVSS (Luo et al. 2024)	CLIP ViT-L/14	Х	-	-	36.2	51.3	28.0	17.9	-	14.2	-
NACLIP (Hajimiri, Ayed, and Dolz 2025)	CLIP ViT-L/14	X	52.1	28.7	29.9	78.6	32.1	21.4	31.4	17.3	36.4
ClearCLIP (Lan et al. 2024a)	CLIP ViT-L/14	X	48.6	28.0	28.6	84.8	31.5	21.2	32.1	16.9	36.5
SC-CLIP (Bai et al. 2024)	CLIP ViT-L/14	Х	<u>65.0</u>	<u>36.9</u>	<u>40.5</u>	<u>88.3</u>	<u>40.6</u>	<u>26.9</u>	41.3	<u>21.7</u>	45.2
RF-CLIP (Ours)	CLIP ViT-L/14	Х	65.8	36.7	41.8	89.1	40.2	26.7	41.4	22.4	45.4
with PAMR			68.1	38.1	42.0	89.1	40.8	27.8	43.0	23.4	46.5

Table 2: Quantitative evaluation on standard benchmarks (unit: %). †: Re-implementation with OpenAI's weights. ‡: Re-implementation with its DINO-B/16 variant. *PAMR*: Pixel-adaptive mask refinement (Araslanov and Roth 2020). Here, the best results are shown in bold and the second-best results are underlined.

Model	FLOPs(G)↓	$Params(M) \!\!\downarrow$	Speed(FPS)↑	mIoU(%)↑
baseline	16.7	149.6	12.7	58.1
CLIP	17.4	149.6	12.0	18.6
ProxyCLIP	34.1	235.4	6.1	59.1
RF-CLIP (Ours)	<u>17.1</u>	149.6	12.0	64.8

Table 3: Efficiency analysis on VOC21 benchmark. **Baseline**: Attn_{kk}-proxy CLIP as the same in Table 1.

2014), Context59 (Mottaghi et al. 2014), COCO-Suff (Caesar, Uijlings, and Ferrari 2018), COCO-Obj (Caesar, Uijlings, and Ferrari 2018), ADE20K (Zhou et al. 2019) and Cityscapes (Cordts et al. 2016). Performance is measured using mean *Intersection-over-Union* (mIoU). All experiments are implemented in PyTorch (Paszke 2019) with MM-Segmentation (Contributors 2020). We employ CLIP models with ViT-B/16 and ViT-L/14 architectures, and set β to 0.7. Evaluation configurations include: sliding window inference with a 224×224 window and a 112×112 stride, input resolution resizing with a short side of 336 (560 for Cityscapes), and text descriptions $\{T_i\}_{i=1}^{N_c}$ constructed by combining standard ImageNet prompts (Radford et al. 2021) with category names. See Appendix for more details.

System level comparison. To evaluate the performance of our proposed method, we compare it with unsupervised approaches, including both training-free and pre-training modes. As shown in Table 2, quantitative evaluation results demonstrate that: 1) Our method achieves the SOTA perfor-

	Components	VOC21	COCO-Stuff	Cityscapes	ADE20K	Avg.
(I)	baseline	59.1	23.6	32.1	16.9	32.9
(II)	mean filtering	58.8	21.4	31.6	14.7	31.6
(III)	(II) + Dis Loc.	60.3	24.4	33.6	17.5	34.0
(IV)	(III) + Attn Red.	61.5	24.8	35.3	18.3	35.0
(V)	(III) + Embed Red.	62.1	25.2	36.7	18.9	35.7
(VI)	(IV) + (V)	63.2	25.4	38.5	19.3	36.6
(VII)	(VI) + Def Loc.	64.8	26.3	41.3	20.4	38.2

Table 4: Effect of different components (unit: %). **Baseline**: layer-averaged key-key attention $\overline{\text{Attn}}_{kk}$ -proxy CLIP. **Dis Loc.**: Distractor localization. **Attn Red.**: Attention weight redistribution. **Embed Red.**: Embedding weight redistribution. **Def Loc.**: Defocus localization.

mance, outperforming same-baseline approaches by 1.6% mIoU and even surpassing methods incorporating additional visual foundational models (VFMs) by +1.1% mIoU; 2) While methods like FreeDa (Barsellotti et al. 2024) and CASS (Kim et al. 2025) achieve SOTA results on specific benchmarks, they exhibit some performance drops on others. In contrast, our approach maintains top-2 performance across all benchmarks, highlighting superior generalization and robustness; 3) Without utilizing the post-processing module, i.e., PAMR (Araslanov and Roth 2020), our method remains highly competitive and still achieves SOTA performance against same-baseline approaches.

Efficiency analysis. To verify the efficiency of our method, we conduct efficiency analysis on an NVIDIA RTX 3090 GPU. As shown in the Table 3, our approach achieves

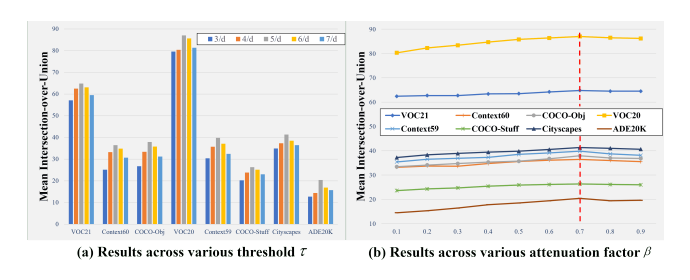


Figure 6: Quantitative results under various threshold and attenuation factor across eight benchmark datasets.

46.2% higher mIoU while maintaining inference speed comparable to CLIP. Compared with ProxyCLIP (Lan et al. 2024b) which introduces an additional VFM, our method doubles the inference speed while improving mIoU by 5.7%. In summary, these results demonstrate that our method achieves the optimal performance-efficiency trade-off.

Components analysis. To validate the effectiveness of the proposed components, we adopt layer-averaged key-key attention $\overline{\mathrm{Attn}}_{kk}$ -proxy CLIP as the baseline (I), and then incrementally integrate our components to measure performance gains. As shown in Table 4, we first perform 3×3 mean filtering on 10 randomly-selected tokens (II), and then the performance drops by 1.3% mIoU compared to the baseline. In contrast, performing same operation on distraction tokens improves performance by 1.1% mIoU (III). These two controlled experiments establish the importance of distraction-aware processing. Next, we reallocate the abundant attention resources from distraction tokens to all non-distraction tokens (IV, V, VI), yielding progressive mIoU gains of +2.1%, +2.8%, and +3.7%. This demonstrates the importance of reallocating the abundant resources occupied by distraction tokens. Finally, defocus localization (VII) directs these liberated resources to target regions, providing an additional +1.6% mIoU improvement. Cumulatively, our components deliver +1.1%, +2.6%, and +1.6%mIoU gains per stage (total +5.3% mIoU), confirming their effectiveness.

Threshold τ analysis. The threshold setting directly impacts the selection of distraction tokens. Intuitively, a lower threshold yields more distraction tokens, consequently increasing the false positive rate; conversely, a higher threshold generates fewer distraction tokens, thus elevating the false negative rate. To investigate appropriate threshold configurations, we conducted exploratory experiments with a range of threshold values across eight benchmarks. Figure 6 (a) demonstrates that setting $\tau=5/d$ achieves optimal performance across all benchmarks; moreover, the performance degradation under low thresholds is significantly more pronounced than under high thresholds, indicating a preference for prioritizing the avoidance of false positives (misclassifying normal tokens as distraction tokens) over false negatives (overlooking distraction tokens) in optimization.

Similarity matrix selection on defocus localization. The similarity matrix assigns weights between nodes and criti-

	Variants	VOC21	COCO-Stuff	Cityscapes	ADE20K	Avg.				
	similarity matrix selection on defocus localization									
(I)	$Attn_{qk}^l$	63.1	25.7	38.8	19.7	36.8				
(II)	$Attn_{qq}^{\hat{l}}$	63.5	26.0	40.2	19.1	37.2				
(III)	$\operatorname{Attn}_{kk}^{l}$	64.0	26.1	40.9	19.6	37.7				
(IV)	$\operatorname{A\overline{t}tn}_{kk}^l$	64.8	26.3	41.3	20.4	38.2				
		graj	oh cut threshold	analysis						
(I)	Otsu.	64.5	26.3	41.1	19.5	37.9				
(II)	Mean.	64.8	26.3	41.3	20.4	38.2				
	emb	edding red	istribution's rec	eptive field an	alysis					
(I)	3×3	64.8	26.3	41.3	20.4	38.2				
(II)	5×5	63.5	25.1	39.7	19.3	36.9				
(III)	7×7	62.2	25.0	38.4	18.7	36.1				

Table 5: Effect of different strategy for our components (unit: %). $\operatorname{A\bar{t}tn}_{kk}^l$: The averaged Attn_{kk} of all layers preceding the current layer. **Otsu.**: An automatic threshold selection technique (Otsu et al. 1975). **Mean.**: Setting the mean value $\frac{1}{N}\sum_{j=1}^N y_1^l[j]$ as the threshold.

cally influences the outcomes of graph cut. As shown in Table 5, the performance comparison across various matrices indicates that distinct self-attention matrices induce subtle performance variations; however, averaging across all preceding layers generates a more robust similarity measure, leading to enhanced overall performance.

Graph cut threshold analysis. Table 5 presents the performance comparison of two threshold-setting methods: Otsu (Otsu et al. 1975) and mean value $\frac{1}{N}\sum_{j=1}^{N}\boldsymbol{y}_{1}^{l}[j]$. The results demonstrate that setting the threshold to $\frac{1}{N}\sum_{j=1}^{N}\boldsymbol{y}_{1}^{l}[j]$ yields the optimal performance.

Embedding redistribution's receptive field analysis. In Equation 13, we employ a 3×3 neighborhood. Table 5 compares performance across different neighborhood sizes, demonstrating that larger neighborhoods degrade performance. This indicates that distraction tokens are likely concentrated in high-frequency regions, making a smaller receptive field more effective for capturing their characteristics.

Attenuation factor β analysis. The attenuation factor β in Equation 9 governs the allocation of attention resources to defocused tokens; a higher value results in more resources being assigned. Figure 6 (b) displays the quantitative analysis for different β , indicating that the optimal performance is achieved at $\beta=0.7$.

Conclusion

In this work, we systematically investigate CLIP's internal mechanisms. Our findings reveal that shallow-layer features exhibit strong spatial coherence and high target saliency; however, in deep layers, distraction tokens emerge that consume significant attention resources, thereby disrupting spatial coherence and diverting attention from highly salient target regions. We designate this as the "distraction" phenomenon. Further experiments demonstrate that these dis-

traction tokens originate from excessive activation in specific dimensions; based on this insight, we effectively localize distraction tokens and achieve performance improvements by filtering them out. Inspired by this, we propose RF-CLIP, a training-free approach that redistributes attention resources from distraction tokens back to target regions. RF-CLIP operates through two stages: first, it identifies distraction tokens and defocused target regions; second, it leverages topology-aware attention reallocation to reassign attention resources occupied by distraction tokens to target regions, thereby mitigating model collapse. Comprehensive experimental evaluations demonstrate significant improvements in dense prediction accuracy and inference speed.

Acknowledgments

This work was supported in part by National Natural Science Foundation of China under Grant 62176224, 62176092, 62222602, 62306165, 62172234, 62306165, and 62376233, in part by Science and Technology on Sonar Laboratory under grant 2024-JCJQ-LB-32/07, in part by Xiaomi Young Talents Program award, in part by Natural Science Foundation of Shanghai under Grant 23ZR1420400; and in part by Natural Science Foundation of Chongqing under Grant CSTB2023NSCQ-JQX0007.

Details of "Distraction" Phenomenon

This section primarily supplements the details of the "distraction" phenomenon.

Recent works identifying analogous phenomena. We summarize recent research identifying analogous phenomena: 1) Registers (Darcet et al. 2023) recognizes and characterizes artifacts in feature maps of supervised and selfsupervised Vision Transformer (ViT) networks; these artifacts correspond to high-norm tokens arising during inference, predominantly in background regions with low information content, which are repurposed for internal computations. 2) CLIPtrase (Shao et al. 2024) and DeCLIP (Wang et al. 2025a) posit that these distraction tokens serve as proxies for the [CLS] token and are misinterpreted by CLIP as global patches. The learning process of the [CLS] token intrinsically amplifies the saliency of global patches. While global patches facilitate [CLS] token learning, they substantially undermine inter-patch semantic correlations. This impairment of semantic correlation proves particularly detrimental for dense feature tasks such as semantic segmentation. Consequently, this likely constitutes a primary reason for CLIP's inherent unsuitability in directly processing dense feature tasks.

The difference in perspective. We delineate key distinctions between our insights and prior research: 1) We posit that these outlier tokens occupying substantial attention resources stem from CLIP's inherent characteristics-specifically, CLIP's tendency to excessively activate certain tokens in particular channels, a data-agnostic process. Thus, these tokens manifest not merely within background regions; 2) We contend that rather than solely proxying [CLS] tokens for global representation, these tokens Algorithm 1: RF-CLIP (take the *l*-th layer as an example)

Input: Visual embeddings $f^l \in \mathbb{R}^{N \times d}$ of layer l

Parameter: Distraction dimension \mathcal{D}_{dis} , threshold τ , head number H

Output: f^{l+1} after updated

- 1: Calculate maximum embeddings weights for each visual tokens: $\phi^l \in \mathbb{R}^N \leftarrow \max_{j \in \mathcal{D}_{dis}} \frac{\boldsymbol{f}^l[:,j]}{\sum_{k=1}^d \boldsymbol{f}^l[:,k]}$. 2: Calculate the averaged *key-key* attention of all layers
- preceding layer l: Attn $_{kk}^l$ $\leftarrow \frac{1}{l \cdot H} \sum_{i,j=1}^{i,j=l,H} \operatorname{Attn}_{kk}^{i,j}$.

 3: Locate distraction tokens: $\mathcal{T}_{dis} \leftarrow (\phi^l > \tau)$. And locate
- defocused tokens: $\mathcal{T}_{def} \leftarrow (\boldsymbol{y}_1^l > \frac{1}{N} \sum_{i=1}^N \boldsymbol{y}_1^l[i]).$ 4: Attention redistribution according to Equation 9 and 11.
- 5: Forward propagation according to Equation 1 and 2.
- 6: Embedding redistribution according to Equation 13 to obtain updated visual embeddings \tilde{f}^{l+1} .
- 7: return $\hat{\boldsymbol{f}}^{l+1}$

Table 6: Quantitative evaluation for four suppression strategies (unit: %). Baseline: Attn_{kk}-proxy CLIP. To non**distraction tokens**: Allocate the redistribution budget Ω to non-distraction tokens. To [CLS] tokens: Allocate Ω to [CLS] tokens. To defocused tokens: Allocate Ω to defocused tokens.

Method	VOC21	COCO-Stuff	Cityscapes	ADE20k	Avg.
baseline	58.1	23.0	31.1	16.3	32.1
To non-distraction tokens	63.2	25.4	38.5	19.3	36.6
To [CLS] token	61.4	23.8	34.3	17.3	34.2
To defocused tokens	64.8	26.3	41.3	20.4	38.2

primarily serve as proxies for foreground target tokens, a finding evidenced in Table 6. After reallocating the attention resources dominated by distraction tokens to the [CLS] token, performance exhibits partial improvement relative to the baseline; however, it underperforms compared to assignment to non-distraction tokens. This indicates that the attention resources consumed by distraction tokens originate not solely from the [CLS] token but also from local image patches, e.g., the foreground regions.

Analysis in CLIP-L/14. In prior sections, we investigated the distribution characteristics of embeddings across dimensions for CLIP-B/16 on three benchmark datasets. In this section, we observe that the same property persists in CLIP-L/14. Specifically, we compute the average vision dense embedding across all layers using a consistent definition approach: $\bar{f} = \frac{1}{L} \sum_{l=1}^{L} (\frac{f^l}{\sum_{j=1}^{d} f^l[:,j]}) \in \mathbb{R}^{N \times d}$. Figure 7 (a) displays the mean embedding weights averaged across the entire dataset, reflecting the weights distribution of the entire dataset in CLIP-L/14's high-dimensional space. We find that three datasets exhibit consistent weights distribution, with several peaks at identical dimensions (e.g., 250, 261, 437, etc., denoted red), which we designate as distraction dimensions \mathcal{D}_{dis} . This distribution is similar in CLIP-B/16. However, the scatter plot of attention weights versus embedding weights (Figure 7(b)) reveals that tokens

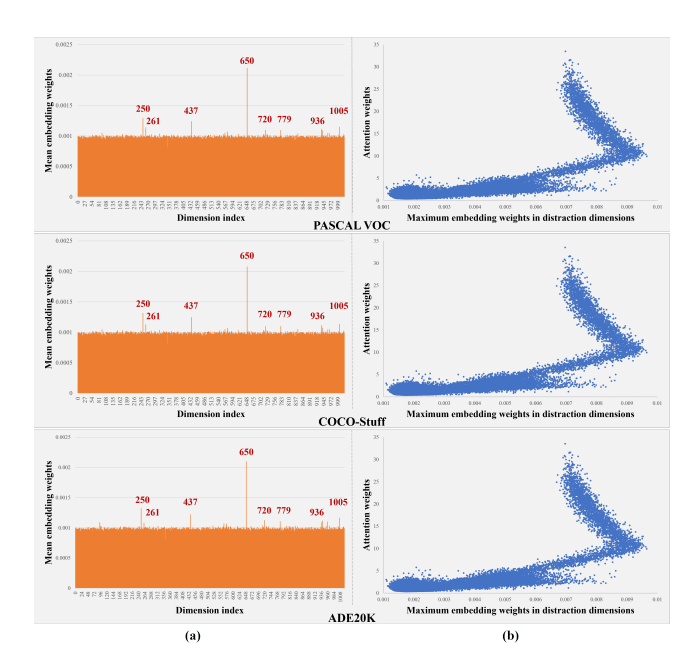


Figure 7: (a) Histogram of per-dimension mean embedding weights averaged across the entire dataset. (b) Scatter plot of all tokens' attention weights versus their maximum embedding weights in distraction dimensions.

dominating high attention resources consistently exhibit elevated embedding weights, whereas tokens with high embedding weights do not necessarily possess substantial attention resources. This characteristic diverges from the behavior observed in CLIP-B/16. Consequently, screening distracting tokens solely based on embedding weights would yield high false positives, necessitating joint evaluation of attention weights for accurate identification: $\phi_i^l > \tau \wedge \sum_j \operatorname{Attn}_{qk}^l[j,i] > 15^3$. We define distraction dimensions: $\mathcal{D}_{dis} = \{4,162,189,326,429,474,633,713\}$ for CLIP-B/16 and $\mathcal{D}_{dis} = \{250,261,437,650,720,779,936,1005\}$ for CLIP-L/14.

More visualization.

This section primarily supplements more visualization analysis for more query-attention(Figure 8), distraction tokens (Figure 9, 10, and 11), corrected attention (Figure 12 and 13), and segmentation results (Figure 14, 15).

More Ablation.

Proxy attention analysis. Our analysis in Table 7 examines the impact of the final-layer proxy self-attention matrix on model performance. The results demonstrate that the layer-wise averaged *key-key* attention mechanism yields superior performance.

Redistribution layer analysis. We investigate whether attention reallocation is required for every layer. Table 7

Table 7: Effect of different strategy for our components (unit: %). $\overline{\text{Attn}}_{qq}$: The averaged Attn_{qq} of all layers. $\overline{\text{Attn}}_{kk}$: The averaged Attn_{kk} of all layers.

	Variants	VOC21	COCO-Stuff	Cityscapes	ADE20K	Avg.			
last layer's proxy attention selection									
(I)	$Attn_{qq}^{L}$	61.1	21.5	35.2	14.3	33.0			
(II)	$Attn_{kk}^{\tilde{L}^{i}}$	63.3	26.1	40.2	19.5	37.3			
(III)	$\overline{\mathrm{Attn}}_{qq}$	63.7	26.4	40.6	19.2	37.5			
(IV)	$\overline{\mathrm{Attn}}_{kk}$	64.8	26.3	41.3	20.4	38.2			
	redistribution layer analysis								
(I)	6	64.1	25.6	41.0	19.5	37.6			
(II)	7	64.0	25.6	40.6	19.5	37.4			
(III)	8	64.1	25.8	40.7	19.6	37.6			
(IV)	9	63.9	25.3	40.5	19.8	37.6			
(V)	10	64.1	25.8	40.8	20.1	37.9			
(VI)	11	64.2	26.0	41.1	20.1	38.0			
(VII)	6 - 12	64.5	26.2	41.1	20.2	38.0			
(VIII)	1 - 12	64.8	26.3	41.3	20.4	38.2			

demonstrates that comprehensive reallocation across all layers yields optimal performance compared to partial layerwise redistribution strategies.

Related Work

Open-Vocabulary Semantic Segmentation. They predominantly dichotomize into two principal paradigms: 1) generative approaches (Gu et al. 2020; Bucher et al. 2019; Cheng et al. 2021; Wu et al. 2023b; Wang et al. 2025b) under transductive learning frameworks, and 2) discriminative methods (Ding et al. 2022; Zhou, Loy, and Dai 2022; Zhou et al. 2023; Xian et al. 2019; Shi, Dao, and Cai 2025) following inductive learning principles. Generative methods fall under transductive methodologies, typically requiring a prior knowledge about unseen categories in open-world scenarios. These techniques (Xian et al. 2019; Bucher et al. 2019; Pastore et al. 2021; Gu et al. 2020) synthesize virtual unseen semantic embeddings by amalgamating visual embeddings with textual semantic embeddings from existing priors. Discriminative approaches constitute inductive methodologies that infer unseen semantics through learned categorical knowledge during training, thereby eliminating the need for prior knowledge about novel categories. State-of-the-art implementations predominantly employ either knowledge distillation (Ding et al. 2022; Xu et al. 2022b; Yu, Seo, and Son 2023; Liang et al. 2023) or feature adaptation strategies (Zhou et al. 2023; Kwon et al. 2023; Xu et al. 2023; Xie et al. 2023; Cho et al. 2023; Li et al. 2024). Knowledge distillation methods typically combine VLMderived image-level semantic discriminability with maskaware segmentation networks to achieve open-vocabulary segmentation, while feature adaptation approaches directly fine-tune VLMs as backbone networks to convert imagelevel classification capabilities into pixel-level discriminative power. Despite remarkable progress, current methodologies exhibit insufficient exploration of latent semantic perception mechanisms.

 $^{^3\}tau = 6/d$

Joint Fine-tuning in OVSS. These methods fine-tune CLIP while training an additional decoder. For instance, CAT-Seg (Cho et al. 2023) proposes an cost-based fine-tuning strategy based on CLIP. MAFT (Jiao et al. 2023) leverages attention bias to finetune CLIP for classification.

Pre Fine-tuning in OVSS. These methods directly fine-tune CLIP using fine-grained vision-language contrastive learning. For example, CLIM (Wu et al. 2024a) employs mosaic augmentation to composite multiple images into a single frame. This arrangement enables each sub-image to serve as a pseudo-region for region-text contrastive learning. Similarly, CLIPSelf (Wu et al. 2023a) enhances CLIP's region-level classification accuracy by maximizing the cosine similarity between the region representations it produces and the representations of their corresponding crops.

Visual Tuning in Vision-Language Models VLM for vision tasks (Radford et al. 2021; Cui et al. 2022; Wu et al. 2021; Lüddecke and Ecker 2022; Wu et al. 2024c, 2025a, 2024b, 2025b) are optimized with a large scale of imagetext pair data on the internet. There are three categories: contrastive, generative, and aligned objectives. CLIP (Radford et al. 2021) first proposes the paradigm of pre-trained vision-language model. DeCLIP (Li et al. 2021) argues that CLIP is data-intensive and proposes a data-efficient training paradigm. UniCL (Yang et al. 2022) combines the two data sources to build a new image-text-label field and proposes unified contrastive learning. ZeroVL (Cui et al. 2022) proposes debiased sampling to deal with biased representation distributions and a new mixup method for the image and text models. OTTER (Wu et al. 2021) uses optimal transport to find the soft label for contrastive learning and handle the problem of noisy image-text pairs. Visual Prompt Learning (Zhou et al. 2022a; Zang et al. 2022; Khattak et al. 2023) is a technique that assists in adapting CLIP-like vision-language models for various visual tasks. CoOp (Zhou et al. 2022b) adopts trainable vectors as word prompt to adapt CLIP for vision classification. VP (Bahng et al. 2022) utilizes perturbations as visual prompt. VPT (Jia et al. 2022) proposes trainable visual prompt to adapt each layer of the visual embeddings. UPT (Zang et al. 2022) constructs unified prompt modeling to extract trainable visual and textual prompt for adapting CLIP. MaPLe (Khattak et al. 2023) adopts trainable prompt to guide both visual and textual embeddings and proposes a coupling function as a bridge to build a multi-modal prompt. DenseCLIP (Rao et al. 2022) uses the contextual information from the image to prompt the language model. Probabilistic prompt (Kwon et al. 2023) applies multiple prompt sampled from probabilistic text embeddings to better understand the image. Seg-Prompt (Zhu et al. 2023) proposes a category-level prompt to improve the model's class-agnostic segmentation ability.

References

Araslanov, N.; and Roth, S. 2020. Single-stage semantic segmentation from image labels. In *Proceedings of the IEEE/CVF conference on computer vision and pattern recognition*, 4253–4262.

Bahng, H.; Jahanian, A.; Sankaranarayanan, S.; and Isola, P. 2022. Exploring visual prompts for adapting large-scale models. *arXiv preprint arXiv:2203.17274*.

Bai, S.; Liu, Y.; Han, Y.; Zhang, H.; and Tang, Y. 2024. Self-calibrated clip for training-free open-vocabulary segmentation. *arXiv* preprint arXiv:2411.15869.

Barsellotti, L.; Amoroso, R.; Cornia, M.; Baraldi, L.; and Cucchiara, R. 2024. Training-free open-vocabulary segmentation with offline diffusion-augmented prototype generation. In *Proceedings of the IEEE/CVF Conference on Computer Vision and Pattern Recognition*, 3689–3698.

Bousselham, W.; Petersen, F.; Ferrari, V.; and Kuehne, H. 2024. Grounding everything: Emerging localization properties in vision-language transformers. In *Proceedings of the IEEE/CVF Conference on Computer Vision and Pattern Recognition*, 3828–3837.

Bucher, M.; Vu, T.-H.; Cord, M.; and Pérez, P. 2019. Zeroshot semantic segmentation. *Advances in Neural Information Processing Systems*, 32.

Caesar, H.; Uijlings, J.; and Ferrari, V. 2018. COCO-Stuff: Thing and stuff classes in context. In *Computer Vision and Pattern Recognition (CVPR)*, 2018 IEEE conference on. IEEE.

Cha, J.; Mun, J.; and Roh, B. 2023. Learning to generate text-grounded mask for open-world semantic segmentation from only image-text pairs. In *Proceedings of the IEEE/CVF Conference on Computer Vision and Pattern Recognition*, 11165–11174.

Cheng, J.; Nandi, S.; Natarajan, P.; and Abd-Almageed, W. 2021. Sign: Spatial-information incorporated generative network for generalized zero-shot semantic segmentation. In *Proceedings of the IEEE/CVF International Conference on Computer Vision*, 9556–9566.

Cho, S.; Shin, H.; Hong, S.; An, S.; Lee, S.; Arnab, A.; Seo, P. H.; and Kim, S. 2023. Cat-seg: Cost aggregation for open-vocabulary semantic segmentation. *arXiv preprint arXiv:2303.11797*.

Cho, S.; Shin, H.; Hong, S.; Arnab, A.; Seo, P. H.; and Kim, S. 2024. Cat-seg: Cost aggregation for open-vocabulary semantic segmentation. In *Proceedings of the IEEE/CVF Conference on Computer Vision and Pattern Recognition*, 4113–4123.

Contributors, M. 2020. MMSegmentation: OpenMMLab Semantic Segmentation Toolbox and Benchmark. https://github.com/open-mmlab/mmsegmentation.

Cordts, M.; Omran, M.; Ramos, S.; Rehfeld, T.; Enzweiler, M.; Benenson, R.; Franke, U.; Roth, S.; and Schiele, B. 2016. The cityscapes dataset for semantic urban scene understanding. In *Proceedings of the IEEE conference on computer vision and pattern recognition*, 3213–3223.

Cui, Q.; Zhou, B.; Guo, Y.; Yin, W.; Wu, H.; Yoshie, O.; and Chen, Y. 2022. Contrastive vision-language pre-training with limited resources. In *European Conference on Computer Vision*, 236–253. Springer.

Darcet, T.; Oquab, M.; Mairal, J.; and Bojanowski, P. 2023. Vision transformers need registers. *arXiv preprint arXiv:2309.16588*.

- Ding, J.; Xue, N.; Xia, G.-S.; and Dai, D. 2022. Decoupling zero-shot semantic segmentation. In *Proceedings of the IEEE/CVF Conference on Computer Vision and Pattern Recognition*, 11583–11592.
- Everingham, M.; Van Gool, L.; Williams, C. K. I.; Winn, J.; and Zisserman, A. 2012. The PASCAL Visual Object Classes Challenge 2012 (VOC2012) Results.
- Gu, Z.; Zhou, S.; Niu, L.; Zhao, Z.; and Zhang, L. 2020. Context-aware feature generation for zero-shot semantic segmentation. In *Proceedings of the 28th ACM International Conference on Multimedia*, 1921–1929.
- Hajimiri, S.; Ayed, I. B.; and Dolz, J. 2025. Pay attention to your neighbours: Training-free open-vocabulary semantic segmentation. In 2025 IEEE/CVF Winter Conference on Applications of Computer Vision (WACV), 5061–5071. IEEE.
- Jia, M.; Tang, L.; Chen, B.-C.; Cardie, C.; Belongie, S.; Hariharan, B.; and Lim, S.-N. 2022. Visual prompt tuning. In *European Conference on Computer Vision*, 709–727. Springer.
- Jiao, S.; Wei, Y.; Wang, Y.; Zhao, Y.; and Shi, H. 2023. Learning mask-aware clip representations for zero-shot segmentation. *Advances in Neural Information Processing Systems*, 36: 35631–35653.
- Kang, D.; and Cho, M. 2024. In defense of lazy visual grounding for open-vocabulary semantic segmentation. In *European Conference on Computer Vision*, 143–164. Springer.
- Khattak, M. U.; Rasheed, H.; Maaz, M.; Khan, S.; and Khan, F. S. 2023. Maple: Multi-modal prompt learning. In *Proceedings of the IEEE/CVF Conference on Computer Vision and Pattern Recognition*, 19113–19122.
- Kim, C.; Ju, D.; Han, W.; Yang, M.-H.; and Hwang, S. J. 2025. Distilling spectral graph for object-context aware open-vocabulary semantic segmentation. In *Proceedings of the Computer Vision and Pattern Recognition Conference*, 15033–15042.
- Kwon, H.; Song, T.; Jeong, S.; Kim, J.; Jang, J.; and Sohn, K. 2023. Probabilistic Prompt Learning for Dense Prediction. In *Proceedings of the IEEE/CVF Conference on Computer Vision and Pattern Recognition*, 6768–6777.
- Lan, M.; Chen, C.; Ke, Y.; Wang, X.; Feng, L.; and Zhang, W. 2024a. Clearclip: Decomposing clip representations for dense vision-language inference. In *European Conference on Computer Vision*, 143–160. Springer.
- Lan, M.; Chen, C.; Ke, Y.; Wang, X.; Feng, L.; and Zhang, W. 2024b. Proxyclip: Proxy attention improves clip for open-vocabulary segmentation. In *European Conference on Computer Vision*, 70–88. Springer.
- Li, J.; Lu, Y.; Xie, Y.; and Qu, Y. 2024. Relationship prompt learning is enough for open-vocabulary semantic segmentation. *Advances in Neural Information Processing Systems*, 37: 74298–74324.
- Li, Y.; Liang, F.; Zhao, L.; Cui, Y.; Ouyang, W.; Shao, J.; Yu, F.; and Yan, J. 2021. Supervision exists everywhere: A data efficient contrastive language-image pre-training paradigm. *arXiv* preprint arXiv:2110.05208.

- Li, Y.; Wang, H.; Duan, Y.; and Li, X. 2023. Clip surgery for better explainability with enhancement in open-vocabulary tasks. *arXiv e-prints*, arXiv–2304.
- Liang, F.; Wu, B.; Dai, X.; Li, K.; Zhao, Y.; Zhang, H.; Zhang, P.; Vajda, P.; and Marculescu, D. 2023. Openvocabulary semantic segmentation with mask-adapted clip. In *Proceedings of the IEEE/CVF Conference on Computer Vision and Pattern Recognition*, 7061–7070.
- Lüddecke, T.; and Ecker, A. 2022. Image segmentation using text and image prompts. In *Proceedings of the IEEE/CVF Conference on Computer Vision and Pattern Recognition*, 7086–7096.
- Luo, J.; Khandelwal, S.; Sigal, L.; and Li, B. 2024. Emergent open-vocabulary semantic segmentation from off-the-shelf vision-language models. In *Proceedings of the IEEE/CVF Conference on Computer Vision and Pattern Recognition*, 4029–4040.
- Mottaghi, R.; Chen, X.; Liu, X.; Cho, N.-G.; Lee, S.-W.; Fidler, S.; Urtasun, R.; and Yuille, A. 2014. The Role of Context for Object Detection and Semantic Segmentation in the Wild. In *IEEE Conference on Computer Vision and Pattern Recognition (CVPR)*.
- Oquab, M.; Darcet, T.; Moutakanni, T.; Vo, H.; Szafraniec, M.; Khalidov, V.; Fernandez, P.; Haziza, D.; Massa, F.; El-Nouby, A.; et al. 2023. Dinov2: Learning robust visual features without supervision. *arXiv preprint arXiv:2304.07193*.
- Otsu, N.; et al. 1975. A threshold selection method from gray-level histograms. *Automatica*, 11(285-296): 23–27.
- Pastore, G.; Cermelli, F.; Xian, Y.; Mancini, M.; Akata, Z.; and Caputo, B. 2021. A closer look at self-training for zero-label semantic segmentation. In *Proceedings of the IEEE/CVF Conference on Computer Vision and Pattern Recognition*, 2693–2702.
- Paszke, A. 2019. Pytorch: An imperative style, high-performance deep learning library. *arXiv preprint arXiv:1912.01703*.
- Radford, A.; Kim, J. W.; Hallacy, C.; Ramesh, A.; Goh, G.; Agarwal, S.; Sastry, G.; Askell, A.; Mishkin, P.; Clark, J.; et al. 2021. Learning transferable visual models from natural language supervision. In *International conference on machine learning*, 8748–8763. PmLR.
- Rao, Y.; Zhao, W.; Chen, G.; Tang, Y.; Zhu, Z.; Huang, G.; Zhou, J.; and Lu, J. 2022. Denseclip: Language-guided dense prediction with context-aware prompting. In *Proceedings of the IEEE/CVF Conference on Computer Vision and Pattern Recognition*, 18082–18091.
- Shao, T.; Tian, Z.; Zhao, H.; and Su, J. 2024. Explore the potential of clip for training-free open vocabulary semantic segmentation. In *European Conference on Computer Vision*, 139–156. Springer.
- Shi, H.; Dao, S. D.; and Cai, J. 2025. LLMFormer: Large language model for open-vocabulary semantic segmentation. *International Journal of Computer Vision*, 133(2): 742–759.
- Shi, J.; and Malik, J. 2000. Normalized cuts and image segmentation. *IEEE Transactions on pattern analysis and machine intelligence*, 22(8): 888–905.

- Shin, G.; Xie, W.; and Albanie, S. 2022. Reco: Retrieve and co-segment for zero-shot transfer. *Advances in Neural Information Processing Systems*, 35: 33754–33767.
- Sun, S.; Li, R.; Torr, P.; Gu, X.; and Li, S. 2024. Clip as rnn: Segment countless visual concepts without training endeavor. In *Proceedings of the IEEE/CVF Conference on Computer Vision and Pattern Recognition*, 13171–13182.
- Wang, F.; Mei, J.; and Yuille, A. 2024. Sclip: Rethinking self-attention for dense vision-language inference. In *European Conference on Computer Vision*, 315–332. Springer.
- Wang, J.; Chen, B.; Li, Y.; Kang, B.; Chen, Y.; and Tian, Z. 2025a. Declip: Decoupled learning for open-vocabulary dense perception. In *Proceedings of the Computer Vision and Pattern Recognition Conference*, 14824–14834.
- Wang, J.; Li, X.; Zhang, J.; Xu, Q.; Zhou, Q.; Yu, Q.; Sheng, L.; and Xu, D. 2025b. Diffusion model is secretly a training-free open vocabulary semantic segmenter. *IEEE Transactions on Image Processing*.
- Wu, B.; Cheng, R.; Zhang, P.; Vajda, P.; and Gonzalez, J. E. 2021. Data efficient language-supervised zero-shot recognition with optimal transport distillation. *arXiv preprint arXiv:2112.09445*.
- Wu, S.; Zhang, W.; Xu, L.; Jin, S.; Li, X.; Liu, W.; and Loy, C. C. 2023a. Clipself: Vision transformer distills itself for open-vocabulary dense prediction. *arXiv* preprint *arXiv*:2310.01403.
- Wu, S.; Zhang, W.; Xu, L.; Jin, S.; Liu, W.; and Loy, C. C. 2024a. Clim: Contrastive language-image mosaic for region representation. In *Proceedings of the AAAI Conference on Artificial Intelligence*, volume 38, 6117–6125.
- Wu, W.; Zhao, Y.; Shou, M. Z.; Zhou, H.; and Shen, C. 2023b. Diffumask: Synthesizing images with pixel-level annotations for semantic segmentation using diffusion models. *arXiv* preprint arXiv:2303.11681.
- Wu, Y.; Kong, X.; Xie, Y.; and Qu, Y. 2025a. RE-GZSL: Relation Extrapolation for Generalized Zero-Shot Learning. *IEEE Trans. Circuits Syst. Video Technol.*, 35(3): 1973–1986.
- Wu, Y.; Xing, M.; Zhang, Y.; Luo, X.; Xie, Y.; and Qu, Y. 2024b. UniDSeg: Unified Cross-Domain 3D Semantic Segmentation via Visual Foundation Models Prior. In *Advances in Neural Information Processing Systems*, 101223–101249.
- Wu, Y.; Xing, M.; Zhang, Y.; Xie, Y.; and Qu, Y. 2025b. Fusion-Then-Distillation: Toward Cross-Modal Positive Distillation for Domain Adaptive 3D Semantic Segmentation. *TCSVT*, 35(9): 9030–9045.
- Wu, Y.; Xing, M.; Zhang, Y.; Xie, Y.; Wu, Z.; and Qu, Y. 2024c. Perturbed Progressive Learning for Semisupervised Defect Segmentation. *IEEE Trans. Neural Networks Learn. Syst.*, 35(5): 6118–6132.
- Wysoczańska, M.; Siméoni, O.; Ramamonjisoa, M.; Bursuc, A.; Trzciński, T.; and Pérez, P. 2024. CLIP-DINOiser: Teaching CLIP a few DINO tricks for open-vocabulary semantic segmentation. In *European Conference on Computer Vision*, 320–337. Springer.

- Xian, Y.; Choudhury, S.; He, Y.; Schiele, B.; and Akata, Z. 2019. Semantic projection network for zero-and few-label semantic segmentation. In *Proceedings of the IEEE/CVF Conference on Computer Vision and Pattern Recognition*, 8256–8265.
- Xie, B.; Cao, J.; Xie, J.; Khan, F. S.; and Pang, Y. 2023. SED: A Simple Encoder-Decoder for Open-Vocabulary Semantic Segmentation. *arXiv preprint arXiv:2311.15537*.
- Xu, J.; De Mello, S.; Liu, S.; Byeon, W.; Breuel, T.; Kautz, J.; and Wang, X. 2022a. Groupvit: Semantic segmentation emerges from text supervision. In *Proceedings of the IEEE/CVF conference on computer vision and pattern recognition*, 18134–18144.
- Xu, M.; Zhang, Z.; Wei, F.; Hu, H.; and Bai, X. 2023. Side adapter network for open-vocabulary semantic segmentation. In *Proceedings of the IEEE/CVF Conference on Computer Vision and Pattern Recognition*, 2945–2954.
- Xu, M.; Zhang, Z.; Wei, F.; Lin, Y.; Cao, Y.; Hu, H.; and Bai, X. 2022b. A simple baseline for open-vocabulary semantic segmentation with pre-trained vision-language model. In *European Conference on Computer Vision*, 736–753. Springer.
- Yang, J.; Li, C.; Zhang, P.; Xiao, B.; Liu, C.; Yuan, L.; and Gao, J. 2022. Unified contrastive learning in image-text-label space. In *Proceedings of the IEEE/CVF Conference on Computer Vision and Pattern Recognition*, 19163–19173.
- Yu, S.; Seo, P. H.; and Son, J. 2023. Zero-shot Referring Image Segmentation with Global-Local Context Features. In *Proceedings of the IEEE/CVF Conference on Computer Vision and Pattern Recognition*, 19456–19465.
- Zang, Y.; Li, W.; Zhou, K.; Huang, C.; and Loy, C. C. 2022. Unified vision and language prompt learning. *arXiv* preprint *arXiv*:2210.07225.
- Zhang, H.; Li, F.; Liu, S.; Zhang, L.; Su, H.; Zhu, J.; Ni, L. M.; and Shum, H.-Y. 2022. Dino: Detr with improved denoising anchor boxes for end-to-end object detection. *arXiv* preprint arXiv:2203.03605.
- Zhou, B.; Zhao, H.; Puig, X.; Xiao, T.; Fidler, S.; Barriuso, A.; and Torralba, A. 2019. Semantic understanding of scenes through the ade20k dataset. *International Journal of Computer Vision*, 127: 302–321.
- Zhou, C.; Loy, C. C.; and Dai, B. 2022. Extract free dense labels from clip. In *European Conference on Computer Vision*, 696–712. Springer.
- Zhou, K.; Yang, J.; Loy, C. C.; and Liu, Z. 2022a. Conditional prompt learning for vision-language models. In *Proceedings of the IEEE/CVF Conference on Computer Vision and Pattern Recognition*, 16816–16825.
- Zhou, K.; Yang, J.; Loy, C. C.; and Liu, Z. 2022b. Learning to prompt for vision-language models. *International Journal of Computer Vision*, 130(9): 2337–2348.
- Zhou, Z.; Lei, Y.; Zhang, B.; Liu, L.; and Liu, Y. 2023. Zegclip: Towards adapting clip for zero-shot semantic segmentation. In *Proceedings of the IEEE/CVF Conference on Computer Vision and Pattern Recognition*, 11175–11185.

Zhu, M.; Li, H.; Chen, H.; Fan, C.; Mao, W.; Jing, C.; Liu, Y.; and Shen, C. 2023. SegPrompt: Boosting Openworld Segmentation via Category-level Prompt Learning. In *Proceedings of the IEEE/CVF International Conference on Computer Vision*, 999–1008.

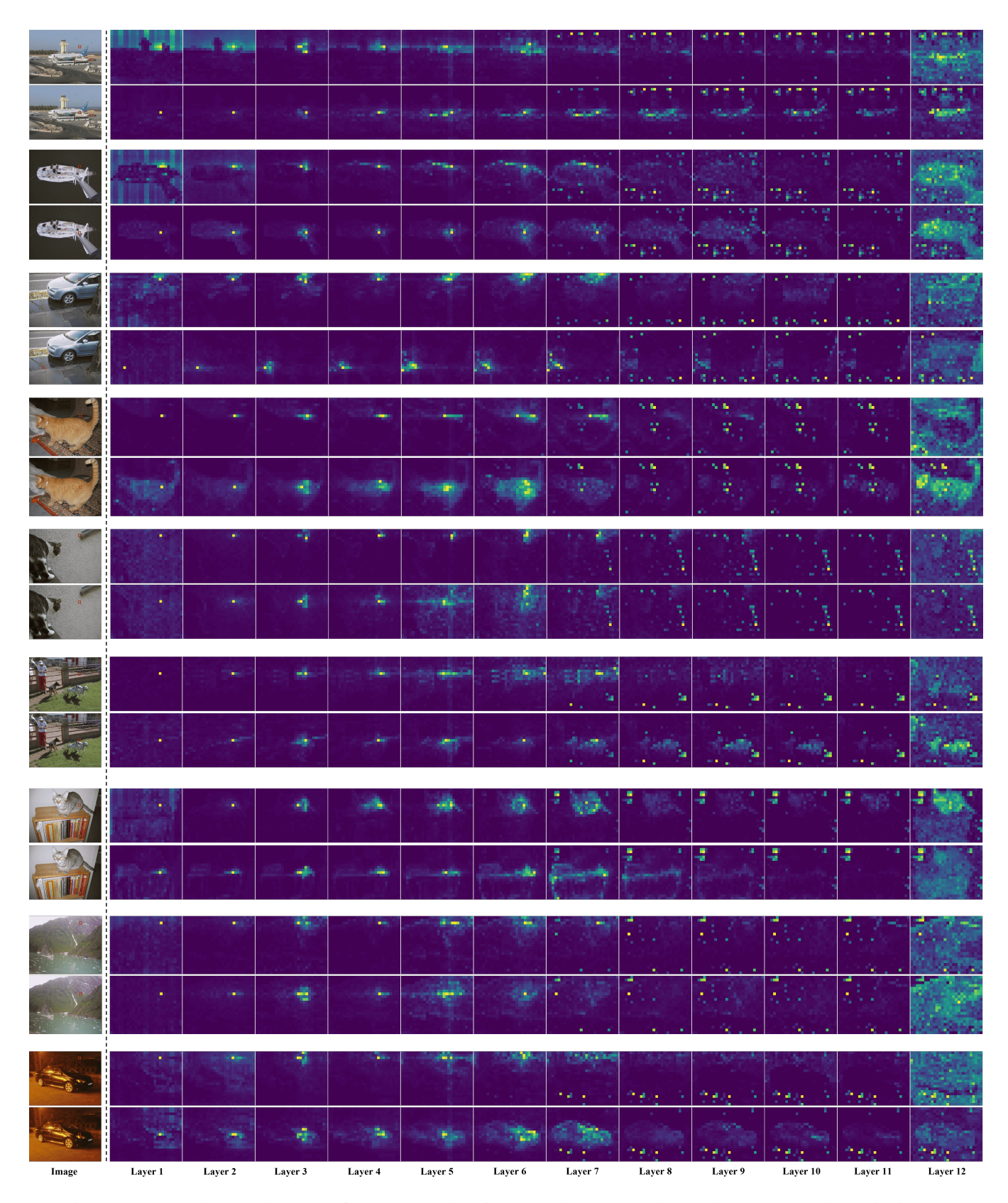


Figure 8: Layer-wise attention maps for two query locations reveal query-to-tokens relevance across the entire image.

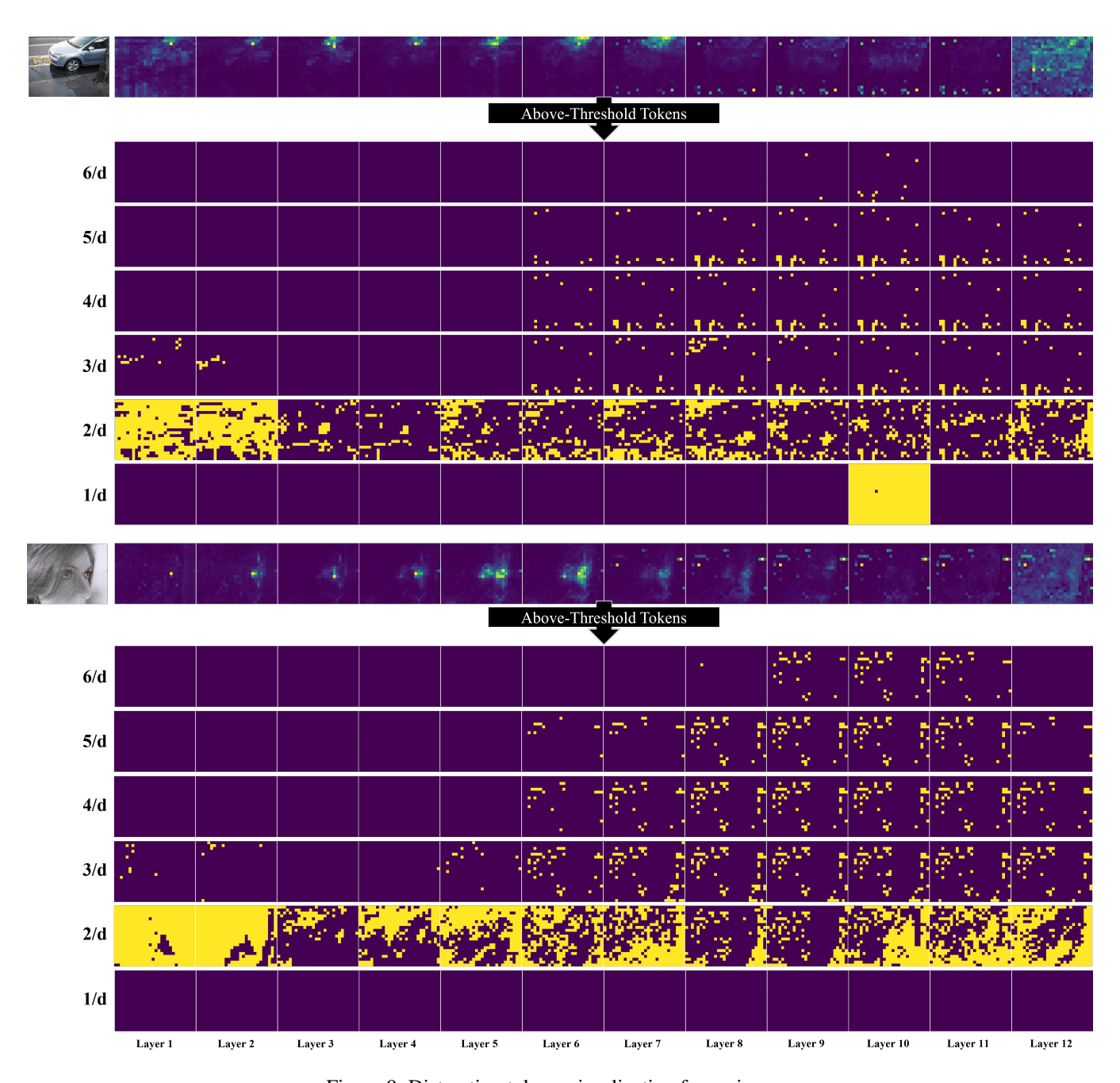


Figure 9: Distraction tokens visualization for various τ .

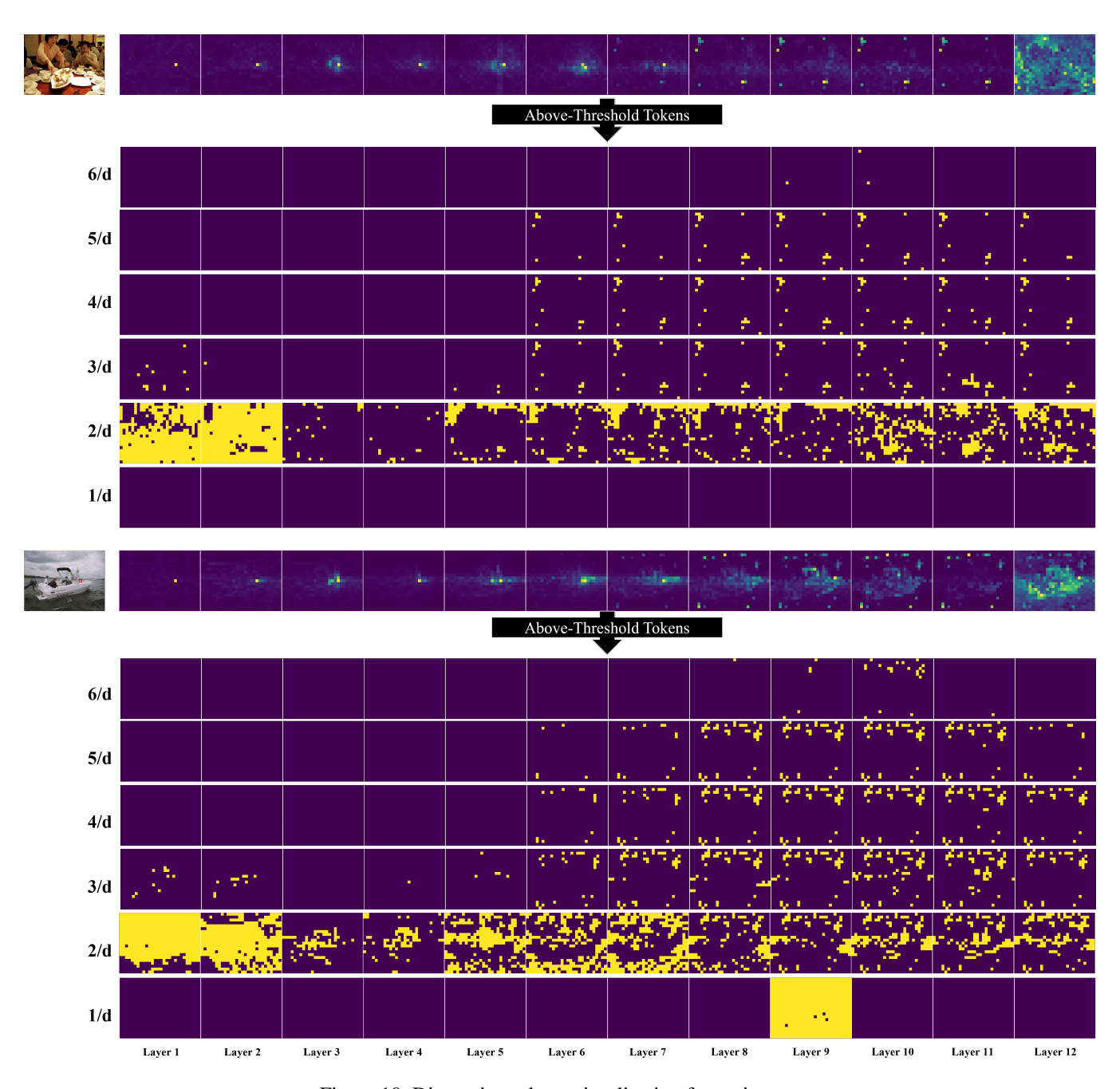


Figure 10: Distraction tokens visualization for various τ .

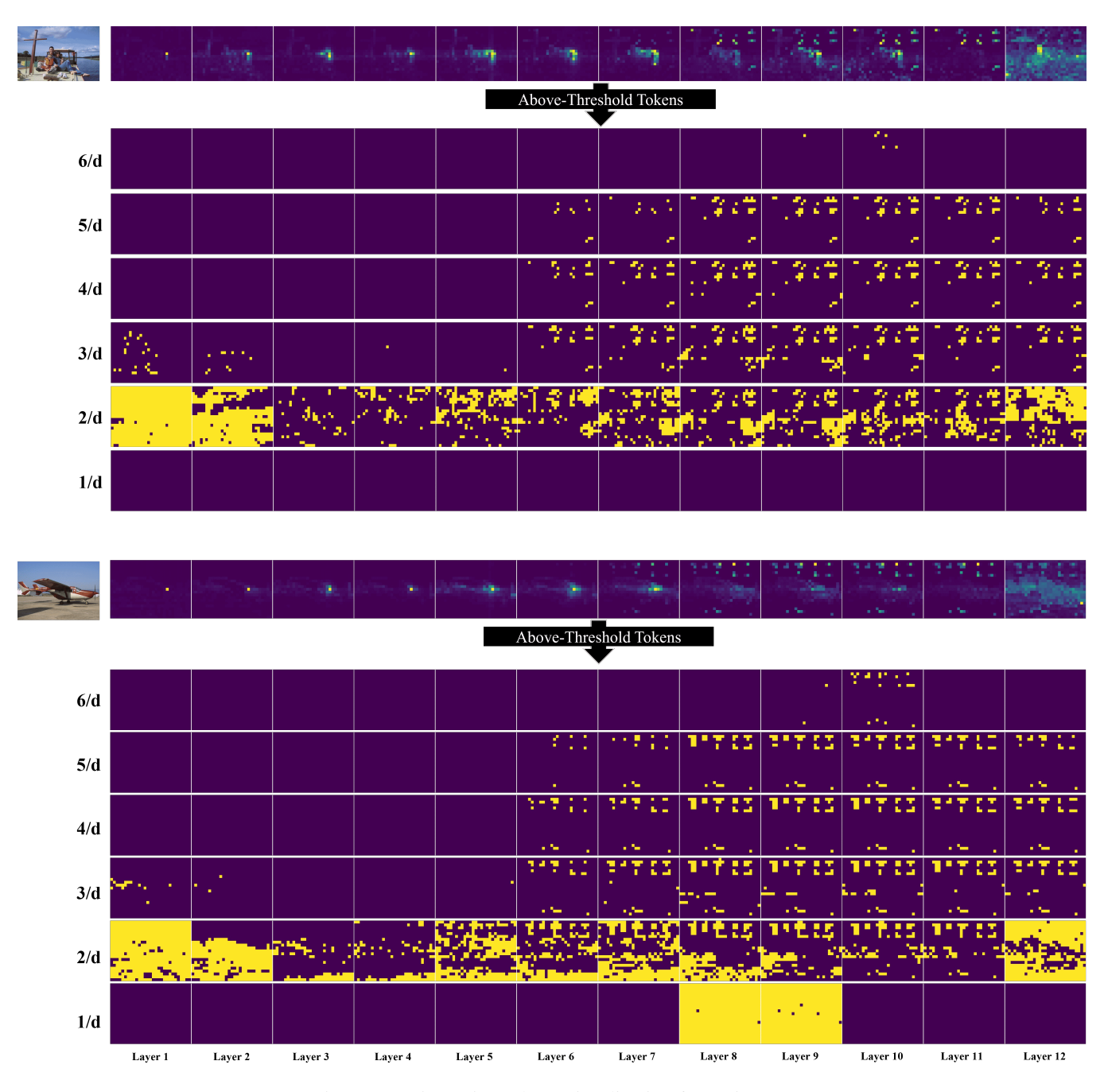


Figure 11: Distraction tokens visualization for various τ .



Figure 12: Query-to-tokens relevance visualization.



Figure 13: Query-to-tokens relevance visualization.

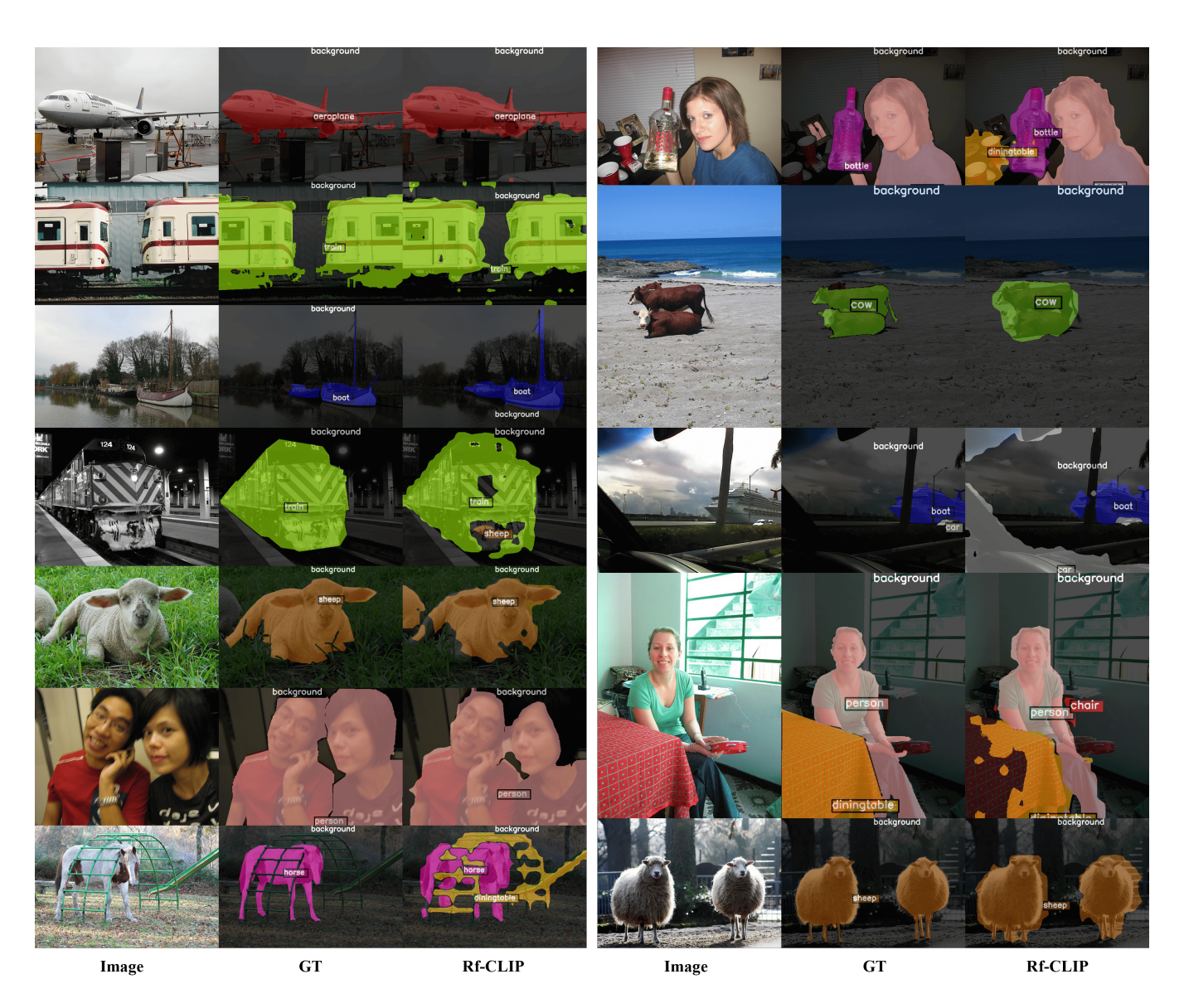


Figure 14: Segmentation visualization on VOC21 benchmark.

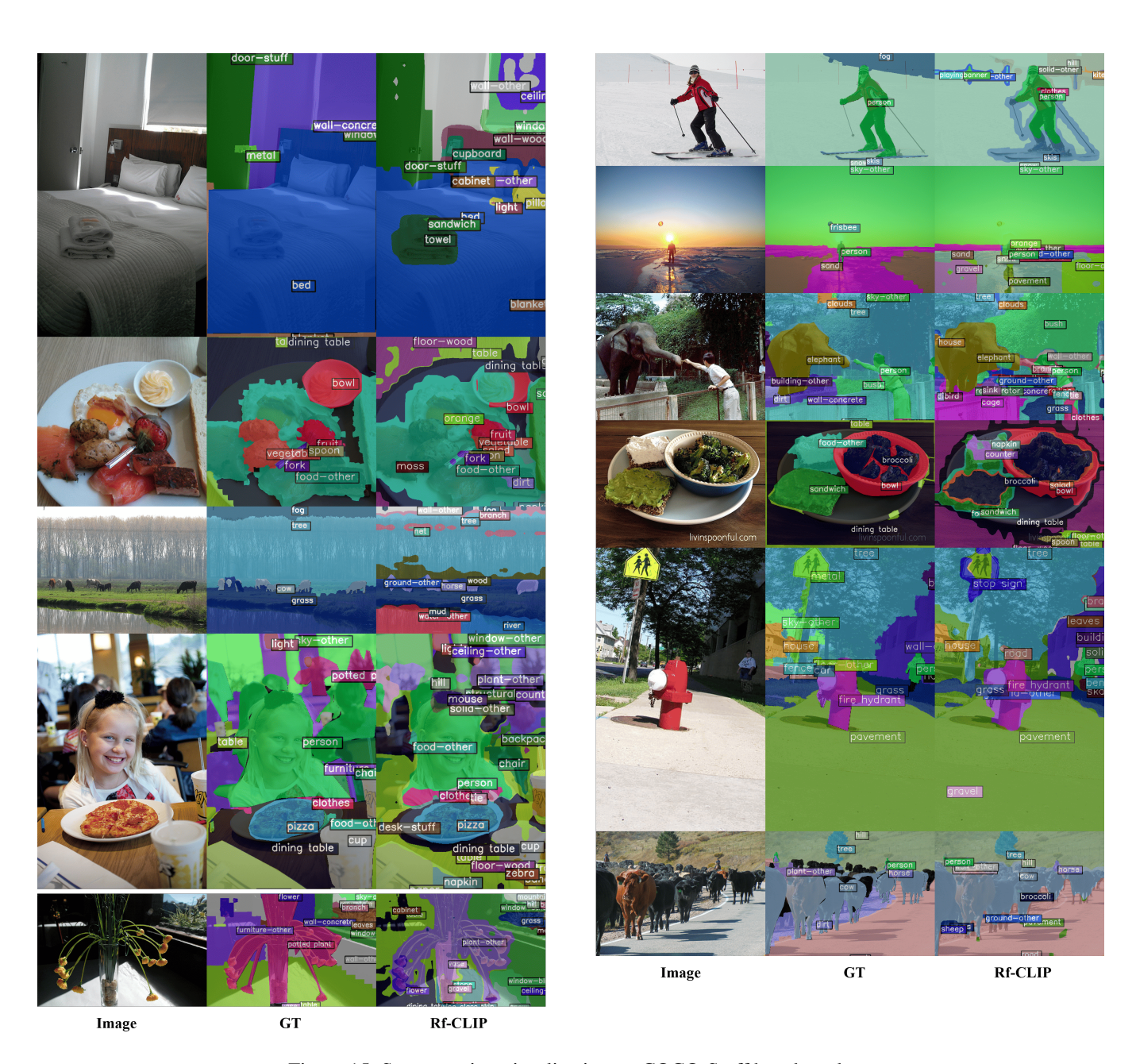


Figure 15: Segmentation visualization on COCO-Stuff benchmark.